Rutherford Backscattering Spectrometry (RBS)

M. Mayer*

Max-Planck-Institut für Plasmaphysik, EURATOM Association,
Garching, Germany

Lectures given at the
Workshop on Nuclear Data for Science and Technology:
Materials Analysis
Trieste, 19-30 May 2003

LNS0822003

*Matej.Mayer@ipp.mpg.de

Abstract

Rutherford Backscattering Spectrometry (RBS) is a widely used method for the surface layer analysis of solids. This lecture gives a brief introduction into the method, and describes scattering kinematics, scattering cross-section data, stopping power data, detector resolution issues, and electronic energy loss straggling in some detail. Computer codes for the simulation of RBS spectra and RBS data analysis are presented, and supply sources of codes and cross-section data are given. Practical applications of RBS and RBS data analysis are demonstrated in some examples.

Contents

1 Introduction

Rutherford Backscattering Spectrometry (RBS) is a widely used nuclear method for the near surface layer analysis of solids. A target is bombarded with ions at an energy in the MeV-range (typically 0.5–4 MeV), and the energy of the backscattered projectiles is recorded with an energy sensitive detector, typically a solid state detector. RBS allows the quantitative determination of the composition of a material and depth profiling of individual elements. RBS is quantitative without the need for reference samples, non-destructive, has a good depth resolution of the order of several nm, and a very good sensitivity for heavy elements of the order of parts-per-million (ppm). The analyzed depth is typically about 2 μm for incident He-ions and about 20 μm for incident protons. The drawback of RBS is the low sensitivity for light elements, which often requires the combination of other nuclear based methods like nuclear reaction analysis (NRA) or elastic recoil detection analysis (ERDA).

Originally E. Rutherford used the backscattering of alpha particles from a gold film in 1911 to determine the fine structure of the atom, resulting in the discovery of the atomic nucleus. RBS as a method for materials analysis was firstly described in 1957 by Rubin et al. [1]. Modern applications of RBS can be found in the book by Tesmer and Nastasi [2], which is also highly recommended for further reading.

RBS includes all types of *elastic* ion scattering with incident ion energies in the range 500 keV – several MeV. Usually protons, ^{4}He, and sometimes lithium ions are used as projectiles at backscattering angles of typically 150–170°. Different angles or different projectiles are used in special cases.

Scattering with non-Rutherford cross-sections or forward scattering is also called RBS – a peculiarity of this well-known acronym. Using *inelastic* scattering and nuclear reactions is called Nuclear Reaction Analysis (NRA), while detection of recoils at forward angles is called Elastic Recoil Detection Analysis (ERD or ERDA). The long history of RBS resulted in a large number and sometimes uncontrolled growth of acronyms - a list of recommended ones can be found in [3], and new acronyms should not be introduced without good reason.

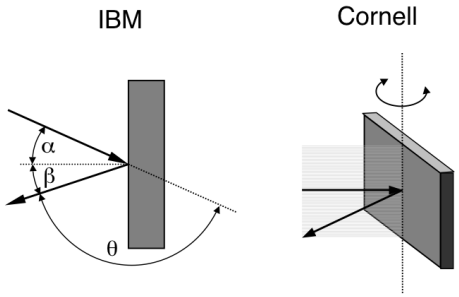

Figure 1: Left: IBM geometry; Right: Cornell geometry. Incident angle α, exit angle β and scattering angle θ.

2 Scattering Geometry and Kinematics

The most often used scattering geometries are shown in Fig. 1. In IBM geometry incident beam, exit beam and surface normal of the sample are in the same plane, with

$$\alpha + \beta + \theta = 180^\circ. \tag{1}$$

In Cornell geometry, incident beam, exit beam and the rotation axis of the sample are in the same plane, and

$$\cos(\beta) = -\cos(\alpha)\cos(\theta). \tag{2}$$

Cornell geometry has the advantage of combining a large scattering angle, which is wishful for optimized mass resolution, and grazing incident and exit angles, which optimizes depth resolution.

The energy E_1 of a backscattered projectile with incident energy E_0 and mass M_1 after scattering is given in the laboratory system by

$$E_1 = KE_0, \tag{3}$$

where the kinematic factor K is given by

$$K = \frac{M_1^2}{(M_1 + M_2)^2}\left\{\cos\theta \pm \left[\left(\frac{M_2}{M_1}\right)^2 - \sin^2\theta\right]^{1/2}\right\}^2. \tag{4}$$

θ is the scattering angle and M_2 the mass of the target nucleus initially at rest. For $M_1 < M_2$ only the plus sign in eq. 4 applies. If $M_1 > M_2$ then

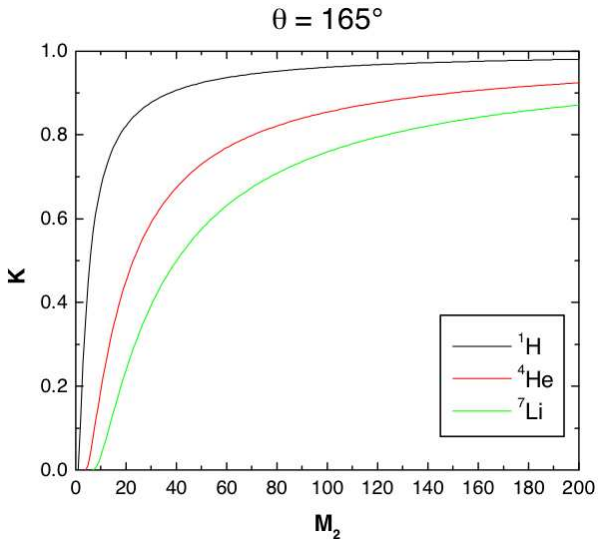

Figure 2: Kinematic factor K at a scattering angle $\theta = 165°$ as a function of target mass M_2 for incident protons, ^{4}He, and ^{7}Li.

eq. 4 has two solutions, and the maximum possible scattering angle θ_{max} is given by

$$\theta_{max} = \arcsin\left(\frac{M_2}{M_1}\right). \tag{5}$$

The kinematic Factor K, as a function of target mass M_2, is shown in Fig. 2 for incident protons, ^{4}He, and ^{7}Li ions at a scattering angle of 165°.

If two different target elements with mass difference ΔM_2 are present, then the energy separation ΔE_1 of particles backscattered from the two masses is given by

$$\Delta E_1 = E_0 \frac{dK}{dM_2} \Delta M_2. \tag{6}$$

As can be seen from Fig. 2, best energy separation and mass resolution are obtained for light target elements where the derivative dK/dM_2 is steep, while for heavy elements the mass resolution gets small. The mass resolution for heavier elements can be improved by using higher incident energies or heavier incident projectiles. However, the deteriorated energy resolution of solid state detectors for heavier ions (see Section 5) generally compensates the increased energy separation, and a gain in mass resolution by using heavier incident ions is only obtained with magnetic or electrostatic spectrometers. With solid state detectors the optimum mass resolution is obtained for

projectiles with mass M_1 in the range 4–7.

3 Scattering Cross-section

3.1 Rutherford cross-section

The Rutherford cross-section for backscattering is given in the laboratory system by

$$\sigma_R\,[\mathrm{mb/sr}] = 5.1837436{\times}10^6 \left(\frac{Z_1 Z_2}{E\,[\mathrm{keV}]}\right)^2 \frac{\left\{\left(M_2^2 - M_1^2\sin^2\theta\right)^{1/2} + M_2\cos\theta\right\}^2}{M_2\sin^4\theta\,\left(M_2^2 - M_1^2\sin^2\theta\right)^{1/2}} \tag{7}$$

θ is the scattering angle, Z_1 and M_1 are the nuclear charge and the mass of the projectile, respectively, and Z_2 and M_2 are the nuclear charge and the mass of the target atom, respectively. σ_R is the differential cross-section in the laboratory system[1]. Experimental measurements indicate that actual cross-sections deviate from Rutherford at both high and low energies for all projectile-target pairs. The low-energy departures are caused by partial screening of the nuclear charges by the electron shells surrounding both nuclei [2, 4, 6]. This screening is taken into account by a correction factor F:

$$\sigma = F\sigma_R$$

For $\theta > 90°$ the correction factor by L'Ecuyer *et al.* [4] is widely used:

$$F_{\mathrm{L'Ecuyer}} = 1 - \frac{0.049\,Z_1 Z_2^{4/3}}{E_{CM}} \tag{8}$$

E_{CM} is the energy in the center of mass system (in keV). Tabulated values of $F_{\mathrm{L'Ecuyer}}$ can be found for example in [2]. The correction for backscattering angles $\theta > 90°$ at typical energies used in ion beam analysis usually is small. For 1 MeV ^{4}He ions on gold the correction is only about 3.5%.

The correction factor by L'Ecuyer (eq. 8) is a first order correction and does not take into account the influence of the scattering angle θ. For $\theta < 90°$ eq. 8 will underestimate the necessary correction to the Rutherford cross-section. At small scattering angles the angular- and energy dependent cor-

[1] For $M_1 > M_2$ there may exist two different solutions of the kinematic equation 4. The cross-section given by eq. 7 applies for the solution with the plus sign.

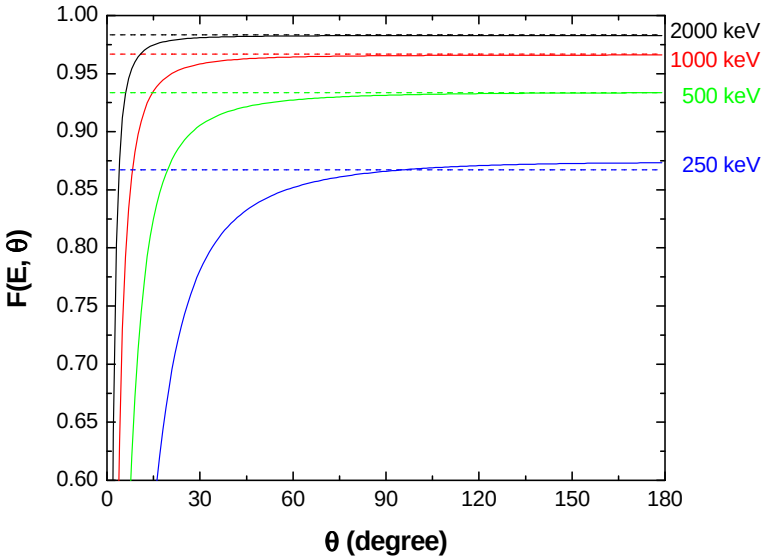

Figure 3: Angular dependence of the correction factors for the Rutherford cross-section by L'Ecuyer (eq. 8, dashed lines) and Andersen (eq. 9, solid lines) for ^{4}He backscattered from gold at different energies.

rection factor by Andersen *et al.* [6] should be used:

$$F_{\text{Andersen}} = \frac{\left(1 + \frac{1}{2}\frac{V_1}{E_{CM}}\right)^2}{\left\{1 + \frac{V_1}{E_{CM}} + \left[\frac{V_1}{2E_{CM}\sin\theta_{CM}/2}\right]^2\right\}^2} \tag{9}$$

θ_{CM} is the scattering angle in the center of mass system. The increase in the kinetic energy V_1 is given by

$$V_1\ [\text{keV}] = 0.04873\, Z_1 Z_2 \left(Z_1^{2/3} + Z_2^{2/3}\right)^{1/2} \quad .$$

The dependence of the correction factor F_{Andersen} from the scattering angle θ for ^{4}He scattered from gold is shown in Fig. 3 for different ^{4}He energies. Dashed lines are the angular independent correction factor by L'Ecuyer. For large scattering angles the correction factors by L'Ecuyer and Andersen are near to unity and similar. However, for small scattering angles the correction by Andersen becomes large and the angle-independent L'Ecuyer correction underestimates the deviations from the Rutherford cross-section.

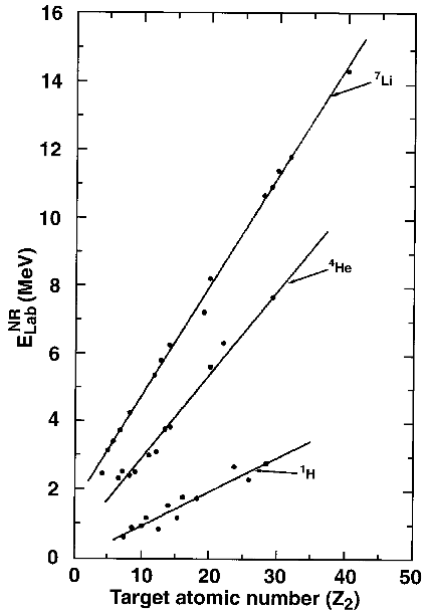

Figure 4: Laboratory projectile energies, E^{NR}_{Lab}, at which backscattering cross-sections deviate from Rutherford by 4% (for $\theta > 160°$) for ^{1}H, ^{4}He and ^{7}Li projectiles. Straight lines result from a least squares fit to experimental or optical model calculation data, see eqs. 10 and 11. From [2].

3.2 Non-Rutherford cross-sections

At high energies the cross-sections deviate from Rutherford due to the influence of the nuclear force. A useful formula above which energy E_{NR} deviations from Rutherford can be expected was given by Bozoian [7, 8, 9]:

$$E^{NR}\,[\mathrm{MeV}] = \frac{M_1 + M_2}{M_2}\frac{Z_2}{10} \quad \text{for } Z_1 = 1 \tag{10}$$

$$E^{NR}\,[\mathrm{MeV}] = \frac{M_1 + M_2}{M_2}\frac{Z_1 Z_2}{8} \quad \text{for } Z_1 > 1 \tag{11}$$

E^{NR} is the energy in the laboratory system, at which the deviation from the Rutherford cross-section gets $> 4\%$. It should be noted, however, that eqs. 10 and 11 are not intended for high accuracy, and deviations up to 500 keV may occur. Threshold energies E^{NR} are shown in Fig. 4 for ^{1}H, ^{4}He and ^{7}Li projectiles and different target atomic numbers Z_2.

As there is no general theory for the calculation of non-Rutherford scattering cross-sections, usually experimental values have to be used. Non-

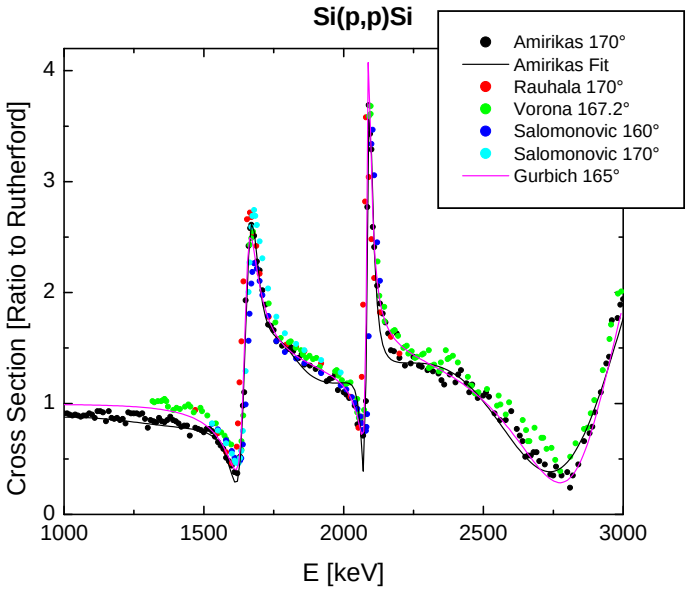

Figure 5: Non-Rutherford backscattering cross-sections for protons from Si at 160° – 170°, as determined by different authors. Dots: Experimental data; Solid lines: Fits to data or theoretical results.

Rutherford scattering cross-sections for many different projectile-target combinations have been measured since 1950 by many authors. As an example the cross-sections for backscattering of protons from silicon at 160° – 170°, as determined by different authors, is shown in Fig. 5 [15]. The discrepancy between different measurements may be up to 30%, and some care has to be applied when cross-section data are used in data evaluation.

Graphical representations of many non-Rutherford scattering cross-sections can be found in [2, 10, 11]. Graphical representations and numerical values can be obtained from SigmaBase [12, 13], or with the program NRABASE [14]. The spectrum simulation program SIMNRA [15] contains many data file with cross-section data, which can be used directly for computer simulations.

4 Stopping Power and Energy Loss

4.1 Stopping power

If an ion beam penetrates through matter it looses energy due to collisions with electrons (electronic stopping) and target nuclei (nuclear stopping). The physics of the energy loss phenomena is complex, and will be not covered in detail here – for more in-depth information see [2, 16].

By traversing a distance Δx in a material the ion beam looses the energy ΔE, where Δx is measured in 10^{15} atoms/cm^2. The stopping power[2] dE/dx is given by $\Delta E/\Delta x \rightarrow dE/dx$, when $\Delta x \rightarrow 0$. As an example the stopping power of ^{4}He ions in Ni is shown in Fig. 6. At low energies (< 100 keV) nuclear stopping due to collision with target nuclei is important, but gets negligible at higher energies. Electronic stopping due to collisions with target electrons is small at low energies, but increases with increasing energy until a maximum in the stopping power is reached. At higher energies the stopping power decreases again. The position of the stopping power maximum depends on incident ion species and target atoms.

Compilations of stopping power data in single elemental targets can be found in [16, 17, 18, 19]. Stopping powers of any ion in any target element (and also many compounds) can be calculated with the program package SRIM [20]. The accuracy of RBS depends strongly on accurate stopping power data. Recent discussions about the accuracy of stopping power models can be found in [21, 22, 23]. Generally, the accuracy of calculated stopping powers for incident protons and ^{4}He ions is about 5%, and about 10% for heavier ions. However, it should be noted that for some elements (especially carbon and silicon) larger deviations may be observed.

4.2 Stopping power in compounds

Usually Bragg's rule [24] is used for the determination of the stopping power in compounds. Bragg's rule is a simple linear additivity rule of the stopping contributions of the different compound elements, assuming that the interaction of an incident ion with a target atom is independent of the surrounding target atoms. For a compound consisting of different elements i with atomic concentrations c_i ($\sum_i c_i = 1$) the total stopping power S is given by

$$S = \sum_i c_i \, S_i \tag{12}$$

[2] Sometimes called stopping cross-section in the literature.

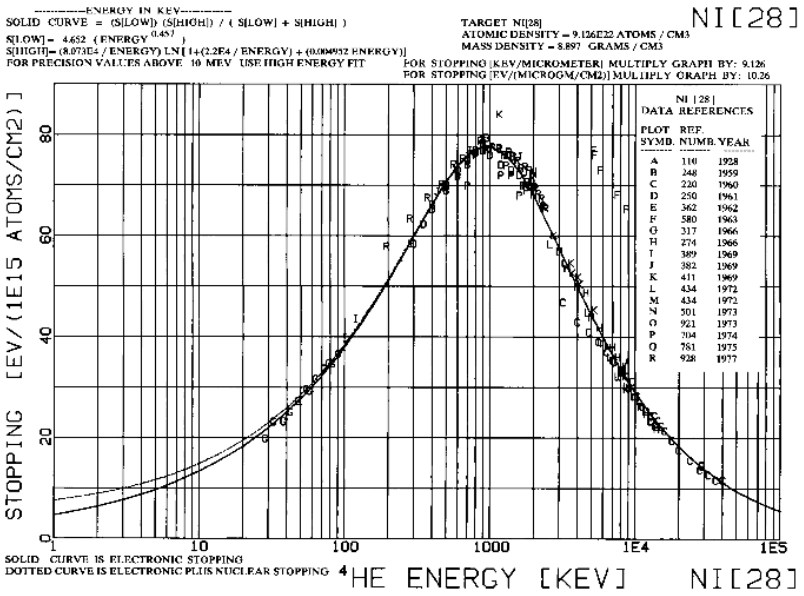

Figure 6: Stopping power of ^{4}He in Ni as a function of ^{4}He energy. Solid line: Electronic stopping power; Dashed line: Electronic + nuclear stopping power. Symbols: Experimental data. From [18].

S_i is the stopping power of each element.

Bragg's rule assumes that the interaction between the ion and the atom is independent of the environment. The chemical and physical state of the medium is, however, observed to have an effect on the energy loss. Deviations from Bragg's rule predictions are most pronounced around the stopping power maximum and for solid compounds such as oxides, nitrides and hydrocarbons. The deviations from Bragg's rule predictions may be of the order of 10–20% [25, 26]. For compounds with heavier atoms such as Fe_2O_3, NbC, NbN, Ta_2O_5, WO_3, Au alloys etc. deviations from Bragg's rule disappear (deviation $< 2\%$) [25, 27].

Ziegler and Manoyan [25] have developed the 'cores and bonds' (CAB) model, which assumes the electronic energy loss to have two contributions: The effect of the atomic cores and the effect of the atomic bonds, such as C-H and C-C. The CAB-model allows better predictions for the stopping in compounds, but the detailed target bond structure has to be known.

4.3 Evaluation of energy loss

The energy E of a particle in the depth x is given by the integral equation

$$E(x) = E_0 - \int_0^{x/\cos\alpha} \frac{dE}{dx'}(E(x'), x')dx' \tag{13}$$

Here we assume that the particle starts with initial energy E_0 at the surface ($x = 0$), $dE/dx'(E(x'), x')$ is the energy and depth dependent stopping power. In principle, eq. 13 can be evaluated directly, but as this consumes a lot of computing time it is not recommended for time-critical computer codes.

For fast evaluation of energy losses Doolittle has developed a much faster algorithm [28]. The beam loses energy according to the differential equation

$$\frac{dE}{dx} = -\epsilon(E) \tag{14}$$

where this is the defining equation for $\epsilon(E)$, the energy dependent stopping cross-section. x is the pathlength into the material, measured in areal density (10^{15} atoms/cm^2). $\epsilon' = d\epsilon/dE$ is the first and $\epsilon'' = d^2\epsilon/dE^2$ the second derivative of the stopping cross-section ϵ.

If incoming or outgoing particles with incident energy E_0 traverse a layer of material with thickness Δx, then the particles energy E_1 after the layer can be expanded into a Taylor series:

$$E_1 = E_0 + \Delta x \frac{dE}{dx}(E_0) + \frac{1}{2}\Delta x^2 \frac{d^2E}{dx^2}(E_0) + \frac{1}{6}\Delta x^3 \frac{d^3E}{dx^3}(E_0) \tag{15}$$

The terms in eq. 15 look as follows:

$$\frac{dE}{dx} = -\epsilon \tag{16}$$

$$\frac{d^2E}{dx^2} = \frac{d}{dx}(-\epsilon) = -\frac{d\epsilon}{dE}\frac{dE}{dx} = \epsilon'\epsilon \tag{17}$$

$$\frac{d^3E}{dx^3} = \frac{d}{dx}(\epsilon'\epsilon) = \frac{d\epsilon'}{dx}\epsilon + \epsilon'\frac{d\epsilon}{dx} = -\epsilon''\epsilon^2 - \epsilon'^2\epsilon \tag{18}$$

With ϵ, ϵ' and ϵ'' evaluated at E_0

$$E_1 = E_0 - \Delta x\epsilon + \frac{1}{2}\Delta x^2\epsilon\epsilon' - \frac{1}{6}\Delta x^3\left(\epsilon''\epsilon^2 + \epsilon'^2\epsilon\right) \tag{19}$$

As was shown in [28], the above equations show a very good accuracy and can be used for fast computation of energy losses, as is necessary in computer simulation codes. The drawback is the need of the first and second derivatives ϵ' and ϵ'' of the stopping power.

5 Silicon Detector Resolution

Usually silicon solid state detectors are used in RBS measurements for the determination of the energy of backscattered particles. The ions create electron-hole pairs in the detector, which are separated by an applied electric field and create a charge pulse. The number of electron-hole pairs is proportional to the ion energy. Limitations to the energy resolution of silicon detectors arise by statistical fluctuations in energy transfer to electrons and phonons and statistical fluctuations in the annihilation of electron-hole pairs.

The energy resolution (full width at half maximum, FWHM) of silicon detectors is shown in Fig. 7 for different ion species. For protons the energy resolution is about 10 keV and almost independent of energy. For He ions the resolution is slightly degraded and an energy dependence is observed, with a resolution of about 12 keV at 2 MeV ion energy. For Li ions an even stronger degradation of the energy resolution occurs, with a resolution of about 20 keV at 5 MeV ion energy. With increasing ion mass and ion energy the resolution degradation increases and limits the applicability of RBS to light ions (protons, helium, lithium), if silicon detectors are used.

An alternative to silicon detectors are electrostatic and magnetic analyzers. They have an excellent energy resolution and do not show a degraded energy resolution for heavy ions, but they are large and expensive. Time-of-flight detectors are another alternative, but they typically have only small solid angles due to the necessary long free flight path. These types of detectors are only used in special cases.

6 Energy Loss Straggling

When a beam of charged particles penetrates matter, the slowing down is accompanied by a spread in the beam energy. This phenomenon is called energy loss straggling. It is due to statistical fluctuations of the energy transfer in the collision processes.

There are four main theories describing electronic energy loss straggling [29, 30, 31], each applicable in a different regime of energy loss. With ΔE the mean energy loss of the beam, and E the energy of the incident beam, we can distinguish:

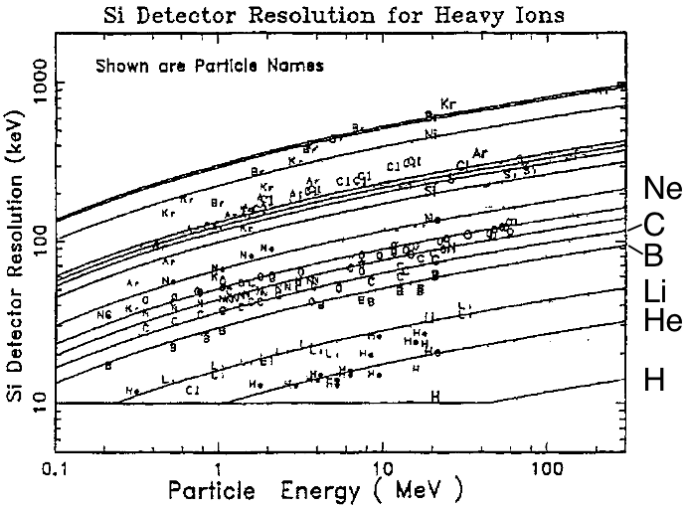

Figure 7: Silicon detector resolution for different ion species as a function of incident energy. From [22].

$\Delta E/E < 10\%$ **Vavilov's Theory** [32, 30]. For thin layers and small energy losses. The energy distribution is non-Gaussian and asymmetrical.

$10 - 20\%$ **Bohr's Theory** [33, 34]. As the number of collisions becomes large, the distribution of particle energies becomes Gaussian.

$20 - 50\%$ **Symon's Theory** [29]. This theory includes nonstatistical broadening caused by the change in stopping power over the particle energy distribution. If the mean energy of the beam is higher than the energy of the stopping power maximum, then particles with a lower energy have a higher stopping power, and particles with higher energy have a smaller stopping power. This results in a nonstatistical broadening of the energy distribution. The width of the particles energy distribution in Symon's theory is significantly higher than predicted by Bohr's theory. The distribution of particle energies is still Gaussian.

$50 - 90\%$ **Payne's and Tschalärs Theory** [35, 36, 37]. When the energy losses become very large and the mean energy of the beam decreases below the energy of the stopping power maximum, the particle energy distribution again becomes skewed, because now particles with lower energy have a lower stopping power than particles with higher energy. The distribution is about Gaussian.

The non-statistic broadening (or skewing) of the energy distribution when penetrating a layer can be calculated in the following way [38]:
Assume two particles with energies E_1 and E_2

$$\begin{aligned} E_1 &= E_0 + \frac{\Delta E}{2} \\ E_2 &= E_0 - \frac{\Delta E}{2} \end{aligned}$$

centered around a mean energy E_0. The energy difference $E_1 - E_2$ of the two particles is ΔE. After penetrating a layer the particles have the energies E_1' and E_2' centered around a mean energy E_0'. The energy difference $\Delta E'$ behind the layer is given by

$$\Delta E' = \frac{\epsilon(E_0')}{\epsilon(E_0)} \Delta E = \frac{\epsilon_f}{\epsilon_i} \Delta E \tag{20}$$

with the stopping power $\epsilon = dE/dx$. ϵ_f is the stopping power at the exit of the layer and ϵ_i the stopping power at the entrance of the layer. If $\epsilon_f > \epsilon_i$, which is the case for all energies above the stopping power maximum, the energy difference increases and the distribution function is broadened. If $\epsilon_f < \epsilon_i$, the energy difference decreases and the distribution function gets skewed. The shape of the distribution remains unchanged: a Gaussian distribution remains gaussian, but the width of the Gaussian is changed according to eq. 20.

To the non-statistic broadening we have to add the statistical effects. When the incident beam with initial energy E_0 and initial beam width σ_0^2 (σ^2 is the variance of the energy distribution, the full width at half maximum (FWHM) is $2\sqrt{2\ln 2}\,\sigma = 2.355\,\sigma$) penetrates a layer of matter with thickness Δx, then the beam width σ_1^2 after penetrating the layer is given by:

$$\sigma_1^2 = \left(\frac{\epsilon_f}{\epsilon_i}\sigma_0\right)^2 + \sigma^2 \tag{21}$$

ϵ_f and ϵ_i are the stopping powers of the material at the entrance and exit of the layer and σ^2 is the energy loss straggling in the layer. The first term in eq. 21 describes the non-statistical broadening of the beam according to eq. 20 due to the energy dependence of the stopping power, the second term adds the statistical effects.

The electronic energy loss straggling can be calculated by applying Chu's theory [39, 34]:

$$\sigma_e^2 = H(E/M_1, Z_2)\sigma_{Bohr}^2 \tag{22}$$

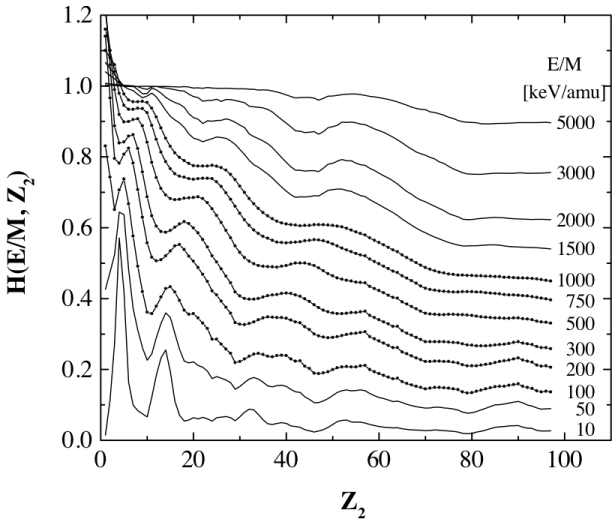

Figure 8: The Chu straggling correction for several values of E/M_1 as a function of the nuclear charge of the target Z_2. Dots are original data from Chu [34], solid lines are extrapolated data taken from [38].

σ^2_{Bohr} is the electronic energy loss straggling in Bohr approximation and is given by [33, 34]:

$$\sigma^2_{Bohr}\ [\mathrm{keV}^2] = 0.26\, Z_1^2\, Z_2\, \Delta x\ [10^{18}\,\mathrm{atoms/cm}^2] \tag{23}$$

Bohr's theory of electronic energy loss straggling is valid in the limit of high ion velocities. In this case the electronic energy loss straggling is almost independent of the ion energy. For lower ion energies the Bohr straggling is multiplied by the Chu correction factor $H(E/M_1, Z_2)$, which depends only on E/M_1 and the nuclear charge of the target atoms Z_2. H takes into account the deviations from Bohr straggling caused by the electron binding in the target atoms. Chu [39, 34] has calculated H by using the Hartree-Fock-Slater charge distribution. This calculation gives straggling values which are considerably lower than those given by Bohr's theory. The correction factor H is shown in Fig. 8. The Z_2 oscillations are clearly visible. The Chu correction is mainly necessary for high Z_2 and low energies. For high energies H approaches 1 and becomes independent of Z_2 and energy.

Fig. 9 compares the beam width (FWHM) of 2.5 MeV ^{4}He ions in silicon calculated by the program SIMNRA [15] using eq. 21 with Bohr's theory. For small energy losses the beam width calculated by SIMNRA is slightly smaller than predicted by Bohr's theory due to the Chu correction. However, this is

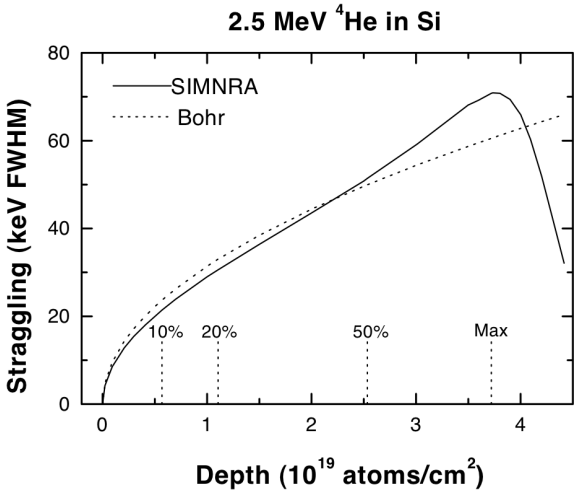

Figure 9: Beam width (FWHM) of 2.5 MeV ^{4}He ions penetrating through silicon. The solid line is the beam width using eq. 21, calculated with the code SIMNRA. The dashed line is the prediction of Bohr's theory. The vertical lines denote the mean depth at which the beam has lost 10%, 20% and 50% of its initial energy. Max denotes the depth at which the mean energy of the beam has decreased to the energy of the stopping power maximum.

counterbalanced by the nonstochastic broadening due to the characteristics of the stopping power curve, and for larger energy losses the beam width gets larger than in Bohr's theory. When the mean beam energy has decreased below the energy of the stopping power maximum, the beam width becomes skewed.

As can be seen from Fig. 8 the deviation of the Chu correction from Bohr's theory is largest for high Z_2 and low energies.

6.1 Energy loss straggling in compounds

For compounds a simple additivity rule for energy loss straggling has been proposed [34]. The straggling in a compound consisting of elements i with atomic concentration c_i ($\sum_i c_i = 1$) is calculated with

$$\sigma^2 = \sum_i c_i \, \sigma_i^2 \tag{24}$$

with σ_i^2 being the straggling in each element.

6.2 Additional straggling contributions

In addition to electronic energy loss straggling the following energy broadening contributions may play a role:

1. Nuclear energy loss straggling due to statistical fluctuations in the nuclear energy loss. Nuclear energy loss straggling is only important for heavy ions.

2. Geometrical straggling due to finite detector solid angle and finite beam spot size, resulting in a distribution of scattering angles and different pathlengths for outgoing particles. Geometrical straggling is important for grazing incident or exit angles and large solid angle detectors.

3. Straggling due to multiple small angle scattering, resulting in angular and energy spread on the ingoing and outgoing paths.

4. Straggling due to surface and interlayer roughness and thickness inhomogeneities of absorber foils.

An additional contribution to the energy broadening visible in experimental spectra is the energy resolution of the detector, see section 5. The different straggling contributions (excluding roughness) have been recently reviewed by Szilágyi *et al.* [38, 40], the influence of surface roughness is discussed in [41].

7 Computer Simulation Codes

During the last two decades several computer codes for the simulation and data evaluation of RBS spectra have been developed, and each code has its own advantages and disadvantages. Often used codes for the simulation of RBS spectra are:

- RUMP by M. Thompson, Cornell University, USA, developed since 1983 [42].

- RBX by E. Kótai, Research Institute for Particle and Nuclear Physics, Hungary, developed since 1985 [43].

- SIMNRA by M. Mayer, Max-Planck-Institute for Plasma Physics, Germany, developed since 1996 [15].

These codes are spectrum simulators, i.e. they calculate a spectrum for a given target structure and allow fitting of target compositions to measured spectra. Other useful programs for designing experimental setups and RBS data analysis are:

- DEPTH by E. Szilágyi allows to calculate the depth resolution of a given experimental setup [44]. This is useful for designing new experiments.
- WiNDF by N. Barradas and C. Jeynes calculates the depth profiles of different elements from a given RBS spectrum [45]. This is useful if one or several elements have a non-uniform depth distribution, for example due to diffusion.

8 Examples

This section shows some examples of typical RBS spectra.

A RBS spectrum of an Ag-layer on TiN on Si substrate is shown in Fig. 10 together with a computer simulation using the SIMNRA code. The experimental spectrum is well reproduced. The structure in the Si spectrum around channel 400 is due to the non-Rutherford scattering cross-section from Si. N is not visible due to overlap with the signal from the Si substrate.

The backscattering spectrum from a Co/Nb multilayer is shown in Fig. 11 together with a computer simulation. The different layers are well separated. Experimental data are well reproduced by the simulation.

The calculated backscattering spectrum from ceramic glass is shown in Fig. 12. The signals from the different elements overlap, and the composition has to be determined from the front edges of the elements.

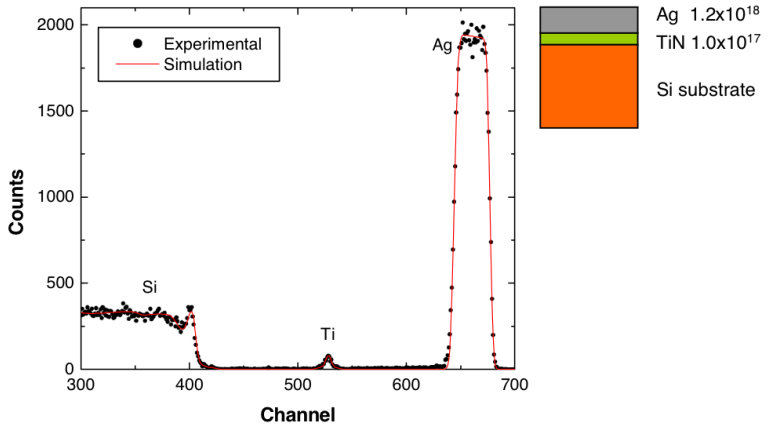

Figure 10: RBS spectrum of an Ag-layer on TiN on Si. The sample structure and the thicknesses of the layers (in atoms/cm^2) are shown schematically. 3.98 MeV ^{4}He, 165° scattering angle. Dots: Experimental data; Solid line: Computer simulation using the SIMNRA code [15].

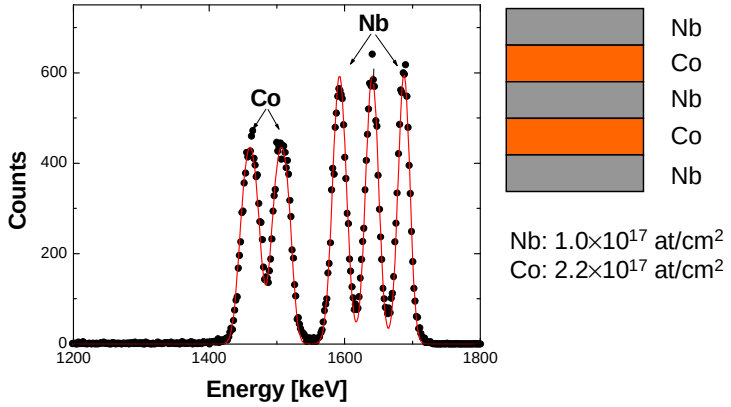

Figure 11: RBS spectrum from a Co/Nb multilayer. The sample structure and the thicknesses of the layers (in atoms/cm^2) are shown schematically. 2.0 MeV ^{4}He, 165° scattering angle. Dots: Experimental data; Solid line: Computer simulation using the SIMNRA code [15].

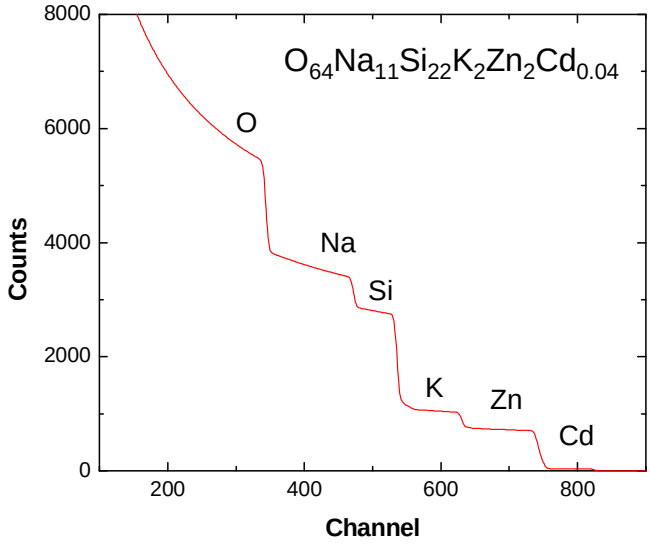

Figure 12: Calculated RBS spectrum of ceramic glass. 1.9 MeV ^{4}He, 170° scattering angle. Computer simulation using the SIMNRA code [15].

Acknowledgments

The data in Fig. 10 were measured by Ch. Linsmeier, IPP Garching, Germany.

References

[1] S. Rubin, T.O. Passell and E. Bailey, Analytical Chemistry 29 (1957) 736.

[2] J.R. Tesmer and M. Nastasi, Eds. *Handbook of Modern Ion Beam Materials Analysis*. Materials Research Society, Pittsburgh, Pennsylvania, 1995.

[3] G. Amsel, Nucl. Instr. Meth. B118 (1996) 52.

[4] J. L'Ecuyer, J.A. Davies and N. Matsunami, Nucl. Instr. Meth. 160 (1979) 337.

[5] M. Hautala and M. Luomajärvi, Rad. Effects 45 (1980) 159.

[6] H.H. Andersen, F. Besenbacher, P. Loftager and W. Möller, Phys. Rev. A21, 6 (1980) 1891.

[7] M. Bozoian, K.M. Hubbard and M. Nastasi, Nucl. Instr. Meth. B51 (1990) 311.

[8] M. Bozoian, Nucl. Instr. Meth. B58 (1991) 127.

[9] M. Bozoian, Nucl. Instr. Meth. B82 (1993) 602.

[10] R. Jarjis, *Nuclear Cross-section Data for Surface Analysis*, vol. 1. University of Manchester, England, 1979.

[11] R. Jarjis, *Nuclear Cross-section Data for Surface Analysis*, vol. 2. University of Manchester, England, 1979.

[12] G. Vizkelethy, Sigmabase: Data base and data server for ion beam analysis. http://ibaserver.physics.isu.edu/sigmabase/.

[13] G. Battistig, Sigmabase (european mirror): Data base and data server for ion beam analysis. http://www.mfa.kfki.hu/sigmabase/.

[14] A. Gurbich, Nrabase: Nuclear reaction data for ion beam analysis. Can be obtained from the SigmaBase Web Site.

[15] M. Mayer, SIMNRA: Simulation of RBS, ERD and NRA spectra. http://www.rzg.mpg.de/∼mam/.

[16] J.F. Ziegler, J.P. Biersack and U. Littmark, *The Stopping and Range of Ions in Solids*, vol. 1 of *The Stopping and Ranges of Ions in Matter*. Pergamon Press, New York, 1985.

[17] H.H. Andersen and J.F. Ziegler, *Hydrogen - Stopping Powers and Ranges in All Elements*, vol. 3 of *The Stopping and Ranges of Ions in Matter*. Pergamon Press, New York, 1977.

[18] J.F. Ziegler, *Helium - Stopping Powers and Ranges in All Elements*, vol. 4 of *The Stopping and Ranges of Ions in Matter*. Pergamon Press, New York, 1977.

[19] H. Paul, http://www.exphys.uni-linz.ac.at/stopping/.

[20] J.F. Ziegler, SRIM: The stopping and range of ions in matter. http://www.srim.org/.

[21] J. Liu, Z. Zheng and W.K. Chu, Nucl. Instr. Meth. B118 (1996) 24.

[22] J.F. Ziegler, Nucl. Instr. Meth. B136-138 (1998) 141.

[23] H. Paul, A. Schinner and P. Sigmund, Nucl. Instr. Meth. B164-165 (2000) 212.

[24] W.H. Bragg and R. Kleeman, Philos. Mag. 10 (1905) 318.

[25] J.F. Ziegler and J.M. Manoyan, Nucl. Instr. Meth. B35 (1988) 215.

[26] D. Boutard, W. Möller and B.M.U. Scherzer, Phys. Rev. B38, 5 (1988) 2988.

[27] D.I. Thwaites, Nucl. Instr. Meth. B27 (1987) 293.

[28] R. Doolittle, Nucl. Instr. Meth. B9 (1985) 344.

[29] M.A. Kumakhov and F.F. Komarov, *Energy Loss and Ion Ranges in Solids*. Gordon and Breach Science Publishers, New York, London, Paris, 1981.

[30] J.R. Bird and J.S. Williams, Eds. *Ion Beams for Materials Analysis*. Academic Press, Sydney, New York, Tokyo, 1989.

[31] J. Tirira, Y. Serruys and P. Trocellier, *Forward Recoil Spectrometry*. Plenum Press, New York, London, 1996.

[32] P.V. Vavilov, Soviet Physics J.E.T.P. 5 (1957) 749.

[33] N. Bohr, Mat. Fys. Medd. Dan. Vid. Selsk. 18, 8 (1948) .

[34] J.W. Mayer and E. Rimini, *Ion Handbook for Material Analysis*. Academic Press, New York, San Francisco, London, 1977.

[35] M.G. Payne, Phys. Rev. 185, 2 (1969) 611.

[36] C. Tschalär, Nucl. Instr. Meth. 61 (1968) 141.

[37] C. Tschalär, Nucl. Instr. Meth. 64 (1968) 237.

[38] E. Szilágy, F. Pászti and G. Amsel, Nucl. Instr. Meth. B100 (1995) 103.

[39] W.K. Chu, Phys. Rev. 13 (1976) 2057.

[40] E. Szilágy, Nucl. Instr. Meth. B161-163 (2000) 37.

[41] M. Mayer, Nucl. Instr. Meth. B194 (2002) 177.

[42] M. Thompson, RUMP: Rutherford backscattering spectroscopy analysis package. http://www.genplot.com.

[43] E. Kótai, RBX: Simulation of RBS and ERD spectra. Can be obtained from the author.

[44] E. Szilágyi, DEPTH: Depth resolution and cross section calculations. Can be obtained from SigmaBase.

[45] N. Barradas and C. Jeynes, WiNDF: Extraction of depth profiles from RBS spectra. http://www.ee.surrey.ac.uk/Research/SCRIBA/ndf/.